ChemComm

COMMUNICATION

View Article Online
View Journal | View Issue

Cite this: *Chem. Commun.*, 2015, 51, 7855

Received 11th February 2015,
Accepted 30th March 2015

DOI: 10.1039/c5cc01195g

www.rsc.org/chemcomm

A core–shell nanohollow-γ-Fe_2O_3@graphene hybrid prepared through the Kirkendall process as a high performance anode material for lithium ion batteries†

Jiangtao Hu,‡ Jiaxin Zheng,‡ Leilei Tian, Yandong Duan, Lingpiao Lin, Suihan Cui, Hao Peng, Tongchao Liu, Hua Guo, Xinwei Wang and Feng Pan*

We synthesized a core–shell structure with graphene as the shell and nano-hollow γ-Fe_2O_3 as the core through a Kirkendall process at room temperature. When this hybrid is used as an anode material for lithium-ion batteries, it exhibits a remarkable electrochemical performance: a high reversible capacity of 1095, 833, and 551 mA h g^{-1} at the current rates of 0.1 C, 1 C, and 2 C, respectively. When evaluated at 10 C, the capacity can still reach 504 mA h g^{-1}.

Lithium ion batteries (LIBs) have found extensive applications in hybrid electric vehicles, electric vehicles, and portable electronic devices, *etc.*[1] Due to their high theoretical and experimental specific capacity, metal oxides, such as Co_3O_4,[2] NiO,[3] SnO_2,[4] Bi_2O_3,[5] GeO_2,[6] CuO,[7] Fe_3O_4,[8] and Fe_2O_3,[9] have been widely investigated as candidates for advanced anode materials. Particularly, with substantial merits of high capacity, environmental friendliness, widespread availability, and enhanced safety, iron oxides are now some of the most promising anodes.[10] However, iron oxides generally bear capacity fading during cycling for its large volume expansion in charge–discharge processes and low rate capacity caused by its poor electronic conductivity.[11] The large volume changes of these anode particles would break the solid electrolyte interface (SEI) and make it re-grow at the solid–liquid interfaces during cycling, leading to poor cycling stability with the Li-ion and electrolyte solution depletion.

One strategy, which succeeds in improving the SEI stability, was to create core–shell or yolk–shell structures, in which the nano-core particles can only expand toward the inside of the shell and the hollows of these core–shell structures are able to balance the volume changes.[12] Thus, to prepare iron oxides with nano-hollow structures to release the stress during volume expansion would be a good method to enhance the cycling performance. There are several well developed approaches (removable templates or template-free) to generate hollow micro/nanostructures. Among them, the Kirkendall effect,[13] which is caused by the differences in diffusion directions and speeds between different ions in the synthesis process, is demonstrated to be a simple, effective, and template-free method. To improve the electronic conduction of these metal oxides, carbon coating on the particle surfaces is a most widely used method.[14] The two dimensional graphene is a well-known carbon allotrope, which possesses high electron mobility and good structure flexibility.[15] Mixing iron oxides with graphene would not only form an electrically conductive network in the anode composite to improve the electrical conductivity greatly but also protect the structure stability in the charge–discharge process. Moreover, graphene could contribute to the total energy storage by its capacitance. However, the final improvement of electrochemical performance introduced by the mixed graphene depends on the mixing or coating method.

Prussian blue (PB) is an important crystalline inorganic–organic hybrid coordinated to rigid organic molecules, which can be used as a novel precursor to prepare various porous micro/nanostructures from zero- to three-dimensions.[16] In this communication, we report a novel method to prepare the core–shell structure with graphene as the shell and nano-hollow γ-Fe_2O_3 as the core (core–shell nano-hollow-γ-Fe_2O_3@graphene) through the nano-scale Kirkendall effect at room temperature. PB is employed as a precursor, and the shell graphene layers are formed on the surface of nano iron particles, which is reduced by glucose with Ar during the heating process. When used as anode materials for lithium-ion secondary batteries, the hybrid anode shows remarkable electrochemical performance: a high reversible capacity of 1095, 833, and 551 mA h g^{-1} at the current rates of 0.1 C, 1 C, and 2 C after 100 cycles, respectively. When evaluated at 10 C, the capacity can still reach 504 mA h g^{-1}.

The core–shell nanohollow γ-Fe_2O_3@graphene was prepared as follows (Scheme 1): the prepared PB precursors were calcined at 650 °C in an argon atmosphere, and Fe nano-metals were produced upon reduction with glucose (step I). After the furnace is cooled naturally to room temperature and then exposed to air, graphene shells were formed and Fe nanoparticles were then oxidized by O_2 by spontaneous combustion to be transformed into nano-hollow

School of Advanced Materials, Peking University Shenzhen Graduate School, Peking University, Shenzhen 518055, China. E-mail: panfeng@pkusz.edu.cn; Tel: +86-755-26033200

† Electronic supplementary information (ESI) available: Details of experimental procedures, XRD patterns, XPS analysis, SEM images, TGA curves, N_2 adsorption results, SEM images and electrochemical testing. See DOI: 10.1039/c5cc01195g

‡ J. Hu and J. Zheng contributed equally to this work.

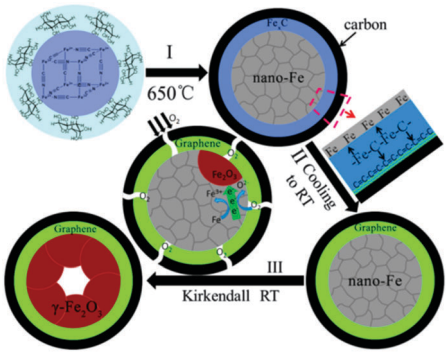

Scheme 1 The schematic illustration of the preparation of the nano-hollow γ-Fe_2O_3@graphene hybrid (RT: room temperature).

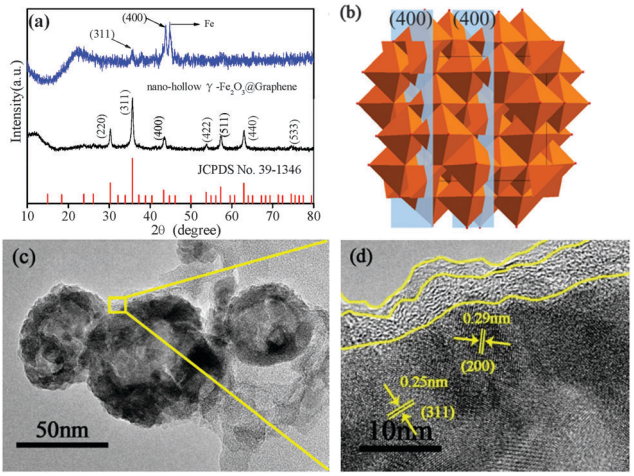

Fig. 1 (a) XRD data of the nano-hollow γ-Fe_2O_3@graphene and the intermediate state; (b) the crystal structure of γ-Fe_2O_3; (c) and (d) TEM images of the nano-hollow γ-Fe_2O_3@graphene.

γ-Fe_2O_3 (step II and III). As a reference, α-Fe_2O_3 was also synthesized by calcining a mixture of PB and glucose in an air atmosphere at 650 °C (Fig. S1, ESI†).

The crystalline structures of the prepared samples were first characterized by X-ray diffraction using Cu Kα radiation (λ = 0.15418 nm) (Fig. 1a). The diffraction peaks at 30.24, 35.63, 43.28, 53.73, 57.27, 62.925, and 62.499° corresponding to crystalline planes of (022), (311), (400), (422), (511), and (440) can be assigned to γ-Fe_2O_3 or Fe_3O_4 (JCPDS No. 39-1346, lattice constant $a = b = c$ = 0.83515 nm).

The XPS peaks of Fe $2p_{3/2}$ and Fe $2p_{1/2}$ for the material are shown in Fig. S2a (ESI†). The peak position of Fe $2p_{3/2}$ is 710.6 eV, which has been reported previously.[17] There is a satellite peak of Fe $2p_{3/2}$ located at 8 eV higher than the main Fe $2p_{3/2}$ peak,[18] indicating that the material contains Fe^{3+} but no Fe^{2+}. Therefore, the prepared samples are proved to be γ-Fe_2O_3. γ-Fe_2O_3 is a nested structure containing FeO_4 tetrahedra and FeO_6 hexahedra, and the (400) peak relates to the face crossing the FeO_4 tetrahedra (Fig. 1b).

The morphology of the γ-Fe_2O_3 particles characterized by TEM, with sizes of about 40–60 nm, is shown in Fig. 1c and d. Noticeably, it shows a core–shell and nano-hollow structure. The core contains many γ-Fe_2O_3 cells (Fig. 1d), which is determined to be about 19 nm

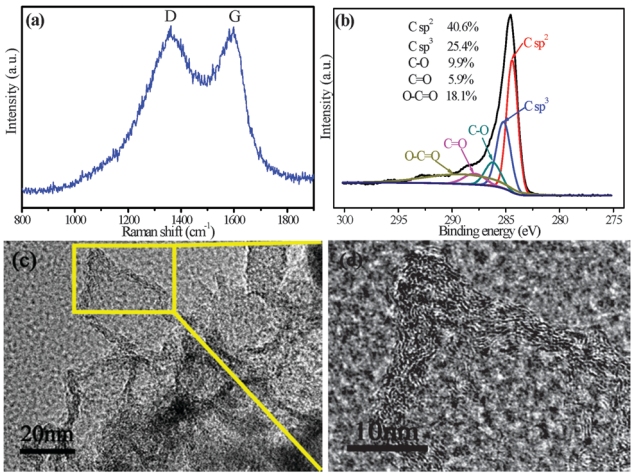

Fig. 2 (a) The Raman spectrum of nano-hollow γ-Fe_2O_3@graphene; (b) C1s spectra of nano-hollow γ-Fe_2O_3@graphene. (c) and (d) TEM images of the shell of the graphene left from nano-hollow γ-Fe_2O_3@graphene dissolved in HCl.

by using the Scherrer equation for the strongest (311) diffraction peak. The Raman spectrum of the nano-hollow γ-Fe_2O_3 hybrid is shown in Fig. 2a. There are two characteristic peaks at 1360 and 1600 cm^{-1}, respectively, corresponding to the D band and G band of carbon (I_D:I_G = 1.0056). The D-band illustrates the defects and disordered portions of carbon, while the G-band stands for the order graphitic crystallites of carbon. The high resolution C1s XPS spectrum of the composite (Fig. 2b) can be fitted into five components, corresponding to carbon atoms in five different chemical environments: carbon sp^2 (284.4 eV), carbon sp^3 (285.2 eV), the carbon in C–O (286.2 eV), the carbonyl carbon (C═O) at 287.9 eV, the carboxylate carbon (O–C═O) at 289.0 eV.[19] The percentage of sp^2 carbon is 40.6%, indicating a high graphitization degree. Therefore, large amounts of graphene-like carbon fragments are formed as the shell on the core nano-hollow γ-Fe_2O_3 particles. When we place the nano-hollow γ-Fe_2O_3@graphene in concentrated hydrochloric acid, the nano-hollow γ-Fe_2O_3 is dissolved and the nano carbon shell is left (Fig. S2b, ESI†), indicating the material with a stable shell structure. From the TEM images of such shell structures (Fig. 2c and d), we can see clearly that the shell consists of thin layers with several nanometers thickness. A large weight loss of γ-Fe_2O_3@graphene about 17.02% between 300 and 450 °C could be seen from the TGA curve (Fig. S3b, ESI†), which can be ascribed to the combustion of graphene with amorphous carbon coated on nano-hollow γ-Fe_2O_3 particles.

Interestingly, the (400) faces are well aligned around and perpendicular to the shell layer of γ-Fe_2O_3 particles (keeping nearly 90° degree with the layer), as shown in Fig. 1d, which would facilitate the Li-ion intercalation/de-intercalation along the (400) planes. To further survey the pore size distribution (PSD) and specific surface area for nano-hollow γ-Fe_2O_3, nitrogen isothermal adsorption measurements were performed (Fig. S3c and d, ESI†). The isothermal curves are regarded as an International Union of Pure and Applied Chemistry (IUPAC) IV type curve, indicating numerous inhomogeneous nanoscale nanopores and mesopores in the samples with a large specific surface area. EDS elemental mapping is shown in

Fig. S4a (ESI†), and the three elements distribute uniformly in this hybrid. The BET specific surface area of the nano-hollow γ-Fe_2O_3@graphene is 203.24 m^2 g^{-1}. It is apparent that the specific surface areas of the mesoporous Fe_2O_3 are much larger than the solid core Fe_2O_3. Such higher surface areas can be attributed to the novel core–shell and nano-hollow structure.

Previous literature also reported that nano-hollow Fe_2O_3 can be obtained by direct decomposition of prussian blue particles. For example, Hu *et al.* first synthesized hollow PB precursors and then sintered them at 250 °C in air to get γ-Fe_2O_3 with hollow structures;[20] Zhang *et al.* first used the prepared PB to react with NaOH solution with different concentrations at room temperature to get $Fe(OH)_3$ microboxes with controllable multishelled structure.[21] Then they sintered the $Fe(OH)_3$ microboxes at 300 °C in air to get γ-Fe_2O_3 with hollow structures. Different from the above two methods, we synthesized the hollow γ-Fe_2O_3 through a simple Kirkendall effect at room temperature. We just sintered the prepared solid PB particles at 650 °C in argon and then cooled the products naturally to room temperature in air. The SEM images of the PB precursor and nano-hollow γ-Fe_2O_3 particles are shown in Fig. S4 (ESI†), we can see that the particle size of PB became smaller (half of the original) after sintering at 650 °C in argon. In order to clarify the synthesis process of nano-hollow γ-Fe_2O_3, we took the crucible out of the quartz tube, and then poured a right amount of alcohol into the crucible to protect O_2 without further oxidation and detected the structure using XRD immediately. Interestingly, the iron peak was observed clearly (Fig. 1a), which explains the spontaneous combustion phenomenon in accordance with the Kirkendall effect with the process (Scheme 1(III)). The Fe atoms first diffuse toward outside, forming an iron layer. At the same time, when the sintered products are brought into contact with the air, oxygen ions would diffuse from the surface toward the inside and oxidize the iron atoms to form the γ-Fe_2O_3 layer on the iron layer. Due to the different diffusion coefficient for Fe atoms and oxygen ions, the nano-hollow structures were produced. The mechanism for the graphene shell formation can be explained as follows: when prussian blue is gradually transformed into nanometer iron during the heating process (Scheme 1(I) and (II)), glucose was decomposed into carbon at the same time, and carbon atoms will gradually seep into the nano iron surface and form carburizing solid solution (Fe_xC, $0 < x < 3$) at high temperature. During the cooling process, carbon atoms would separate out from the carburizing solid solution and form graphene layers on the surface of iron nanoparticles.[22] This graphene shell structure will be kept when the iron nanoparticles are further oxidized to nano-hollow γ-Fe_2O_3.

We next studied the electrochemical properties of such core–shell and nano-hollow γ-Fe_2O_3@graphene composites. The CV curves and the charge–discharge voltage profiles of the nano-hollow γ-Fe_2O_3@graphene electrode are shown in Fig. S5a and b (ESI†).

Rate capabilities were examined next (Fig. 3a and b). Nano-hollow γ-Fe_2O_3@graphene shows rather high rate performance with an average discharge capacity of 1095, 1072, 1022, 974, 902, 704, and 504 mA h g^{-1} at the rate of 0.1, 0.2, 0.5, 1, 2, 5, and 10 C, respectively. These values are much higher than the capacities of γ-Fe_2O_3 reported in other studies[23] (Fig. 3a) and other Fe_2O_3 anodes (including α-Fe_2O_3) at the same current densities (Table 1 (ref. 24)

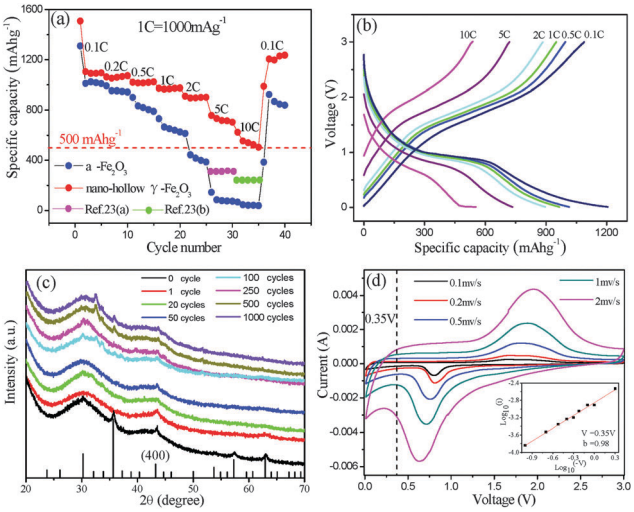

Fig. 3 Electrochemical performance for nano-hollow γ-Fe_2O_3@graphene: (a) rate performances and compared with α-Fe_2O_3, γ-Fe_2O_3@CNTs at 5 C, and γ-Fe_2O_3–rGO hybrids at 10 C; (b) the charge–discharge curves; (c) XRD datas after different cycles; (d) cyclic voltammograms at different sweep rates. The peaks of CV reflect the redox reactions occurred during the electrochemical process but can't reflect the capacitive properties of the battery, so we randomly selected a voltage point (0.35 V) below the peak values and fit the corresponding the logarithmic relationship of the sweep rate and current at this point to derive the capacitive properties (inset).

and Table S1, ESI†). Clear voltage platforms are observed in all the charge and discharge curves (Fig. 3b), corresponding to the process of Li intercalation and de-intercalation. Such excellent rate performance of γ-Fe_2O_3@graphene can be attributed to the structure stability induced by the hollow structure and γ-Fe_2O_3 itself, and the high electrical conductivity induced by the graphene shells. This is also validated by our electrochemical impedance spectroscopy (EIS) measurements (Fig. S6, ESI†). The cycling performance of nano-hollow γ-Fe_2O_3@graphene and α-Fe_2O_3 within a voltage window of 0.01 to 3 V is illustrated in Fig. S7 (ESI†). The nano-hollow γ-Fe_2O_3@graphene electrode reserved 833 and 551 mA h g^{-1} after 100 cycles at the current rate of 1 and 2 C, respectively, demonstrating a good cycling stability.

Interestingly, the (400) peak which is related to the planes crossing the FeO_4 tetrahedra in XRD still exists after 1000 cycles (Fig. 3c), indicating a relatively high structural stability for γ-Fe_2O_3 during the electrochemical cycles. The battery was tested 750 cycles at 10 C, and a capacity of 625 mA h g^{-1} remained when cycled back to 1 C (Fig. S8, ESI†). The (400) peak in γ-Fe_2O_3 was reported previously,[25] but this work is the first time to report that it still exists during the charge and discharge process. This structural stability guarantees the cycling stability with fast Li-ion transport.

Table 1 The comparison of iron-based materials for lithium-ion batteries

Ref.	Material (G: graphene)	Specific capacity (mA h g^{-1})	Rate-capacity (mA h g^{-1})
24*a*	Fe_2O_3/C	0.05 C/623 for 100 cycles	1 C/450
24*b*	Fe_2O_3/C	0.2 C/790 for 100 cycles	4 C/390
24*c*	Fe_2O_3/C	0.5 C/800 for 100 cycles	3 C/420
24*d*	Fe_2O_3/G	0.8 C/711 for 50 cycles	1.6 C/660
24*e*	Fe_2O_3/G	0.2 C/1049 for 450 cycles	2 C/634

In contrast, the capacity of the α-Fe_2O_3 electrode drops heavily during the cycles in our work (400 mA h g^{-1} after 100 cycles at the current rate of 1 C, Fig. S7a, ESI†) and in ref. 22*a*.

The cycling capacity of γ-Fe_2O_3@graphene is about 1050 mA h g^{-1} at 0.1 C (Fig. S9, ESI†), and γ-Fe_2O_3 can contribute 835.81 mA h g^{-1} (83% in weight). The left part could be ascribed to the capacitance from the carbon (graphene and amorphous carbon, 17% in weight in this composite), which is estimated to be 1260 mA h g^{-1}. In fact, we can divide the discharge capacity into two parts by 0.8 V (Fig. S7b, ESI†) and plot the capacity for the two parts with the increasing cycle number in Fig. S9 (ESI†). The capacity above 0.8 V denotes the capacity within the discharge platform, and the capacity below 0.8 V denotes the capacity for the tails in the discharge curve. We can see that the capacity above 0.8 V is on the way down, the capacity below 0.8 V is on the rise with the increasing cycle number. In order to explain this phenomenon, we did a CV test at different rates (Fig. 3d). Assuming that the current obeys a power-law relationship ($i = av^b$), where a and b are adjustable values.[26] If the value of b is equal to 0.5, then we can say that the current is controlled by semi-infinite diffusion. If b is equal to 1, it reflects a capacitive process. Here we got the b-value of 0.98 through fitting the logarithmic relationship of the sweep rate and current at 0.35 V (inset in Fig. 3d), demonstrating that capacitance plays an important role at low voltage (0.8–0.1 V) during the discharge process. We attribute this large contribution from capacitance to the graphene shells around the nano-hollow γ-Fe_2O_3@graphene particles and the huge specific surface areas.

In summary, the nano-hollow γ-Fe_2O_3@graphene with a core–shell structure has been synthesized through the Kirkendall process at room temperature. When used as anode material for LIBs, this hybrid demonstrated a remarkable electrochemical performance: a high reversible capacity of 1095, 833, and 551 mA h g^{-1} at the current rates of 0.1 C, 1 C, and 2 C after 100 cycles, respectively. When evaluated at 10 C, the capacity still can reach 504 mA h g^{-1}. This remarkable performance can be attributed to the novel nano-hollow and core–shell structure and the structure stability of γ-Fe_2O_3 ((400) peak exists all the time). At the same time, the huge contribution of capacitance is verified, which could be ascribed to the huge specific surface area and the tightly coated graphene layers. This synthetic route is simple, low-cost, eco-friendly, and especially combines Li storage with capacitance in energy storage. It enables the modified γ-Fe_2O_3 to be a promising anode material for advanced LIBs.

This research was supported by National Project for EV Batteries (20121110, OptimumNano, Shenzhen), Guangdong Innovation Team Project (No. 2013N080), NSFC (51302007) and Shenzhen Science and Technology Research Grant (No. ZDSY20130331145131323, CXZZ20120829172325895, JCYJ20120614150338154, and JCYJ20130329181509637).

Notes and references

1 (*a*) A. Yoshino, *Angew. Chem., Int. Ed.*, 2012, **51**, 5798; (*b*) P. G. Bruce, B. Scrosati and J. M. Tarascon, *Angew. Chem., Int. Ed.*, 2008, **47**, 2930.
2 B. Li, H. Cao, J. Shao, G. Li, M. Qu and G. Yin, *Inorg. Chem.*, 2011, **50**, 1628.
3 B. Varghese, M. V. Reddy, Y. Zhu, C. S. Lit, T. C. Hoong, G. V. Subba Rao, B. V. R. Chowdari, A. T. S. Wee, C. T. Lim and C. H. Sow, *Chem. Mater.*, 2008, **20**, 3360.
4 C. Kim, M. Noh, M. Choi, J. Cho and B. Park, *Chem. Mater.*, 2005, **17**, 3297.
5 Y. Li, M. A. Trujillo, E. Fu, B. Patterson, L. Fei, Y. Xu, S. Deng, S. Smirnov and H. Luo, *J. Mater. Chem. A*, 2013, **1**, 12123.
6 Y.-M. Lin, K. C. Klavetter, A. Heller and C. B. Mullins, *J. Mater. Chem. A*, 2013, **4**, 999.
7 J. Morales, L. Sánchez, F. Martín, J. R. Ramos-Barrado and M. Sánchez, *Electrochim. Acta*, 2004, **49**, 4589.
8 J. Luo, J. Liu, Z. Zeng, C. F. Ng, L. Ma, H. Zhang, J. Lin, Z. Shen and H. J. Fan, *Nano Lett.*, 2013, **13**, 6136.
9 J. Ma, X. Zhang, K. Chen and X. Han, *RSC Adv.*, 2014, **4**, 9166.
10 (*a*) J. Luo, X. Xia, Y. Luo, C. Guan, J. Liu, X. Qi, C. F. Ng, T. Yu, H. Zhang and H. J. Fan, *Adv. Energy Mater.*, 2013, **3**, 737; (*b*) F. Han, D. Li, W.-C. Li, C. Lei, Q. Sun and A.-H. Lu, *Adv. Funct. Mater.*, 2013, **23**, 1692; (*c*) Z. Wang, L. Zhou and X. W. David Lou, *Adv. Mater.*, 2012, **24**, 1903; (*d*) B. Koo, H. Xiong, M. D. Slater, V. B. Prakapenka, M. Balasubramanian, P. Podsiadlo, C. S. Johnson, T. Rajh and E. V. Shevchenko, *Nano Lett.*, 2012, **12**, 2429; (*e*) B. P. Hahn, J. W. Long, A. N. Mansour, K. A. Pettigrew, M. S. Osofsky and D. R. Rolison, *Energy Environ. Sci.*, 2011, **4**, 1495.
11 (*a*) Z. Wang, D. Luan, S. Madhavi, C. M. Li and X. W. Lou, *Chem. Commun.*, 2011, **47**, 8061; (*b*) Y.-M. Lin, P. R. Abel, A. Heller and C. B. Mullins, *J. Phys. Chem. Lett.*, 2011, **2**, 2885; (*c*) F. Cheng, J. Liang, Z. Tao and J. Chen, *Adv. Mater.*, 2011, **23**, 1695; (*d*) J. Zhang, T. Huang, Z. Liu and A. Yu, *Electrochem. Commun.*, 2013, **29**, 17; (*e*) L. Zhang, H. B. Wu and X. W. D. Lou, *Adv. Energy Mater.*, 2014, **4**, 1300958.
12 (*a*) K. Yan, H. W. Lee, T. Gao, G. Zheng, H. Yao, H. Wang, Z. Lu, Y. Zhou, Z. Liang, Z. Liu, S. Chu and Y. Cui, *Nano Lett.*, 2014, **14**, 6016; (*b*) Z. W. Seh, J. H. Yu, W. Li, P. C. Hsu, H. Wang, Y. Sun, H. Yao, Q. Zhang and Y. Cui, *Nat. Commun.*, 2014, **5**, 5017; (*c*) L. Zhou, H. Xu, H. Zhang, J. Yang, S. B. Hartono, K. Qian, J. Zou and C. Yu, *Chem. Commun.*, 2013, **49**, 8695; (*d*) Z. Padashbarmchi, A. H. Hamidian, H. Zhang, L. Zhou, N. Khorasani, M. Kazemzad and C. Yu, *RSC Adv.*, 2015, **5**, 10304.
13 Y. Yin, R. M. Rioux, C. K. Erdonmez, S. Hughes, G. A. Somorjai and A. P. Alivisatos, *Science*, 2004, **304**, 711.
14 H. Zhang, X. Sun, X. Huang and L. Zhou, *Nanoscale*, 2015, **7**, 3270.
15 (*a*) S. Stankovich, D. A. Dikin, G. H. B. Dommett, K. M. Kohlhaas, E. J. Zimney, E. A. Stach, R. D. Piner, S. T. Nguyen and R. S. Ruoff, *Nature*, 2006, **442**, 282; (*b*) E. Yoo, J. Kim, E. Hosono, H.-S. Zhou, T. Kudo and I. Honma, *Nano Lett.*, 2008, **8**, 2277; (*c*) C. Wang, D. Li, C. O. Too and G. G. Wallace, *Chem. Mater.*, 2009, **21**, 2604.
16 S. Xiang, W. Zhou, Z. Zhang, M. A. Green, Y. Liu and B. Chen, *Angew. Chem., Int. Ed.*, 2010, **49**, 4615.
17 T. Yamashita and P. Hayes, *Appl. Surf. Sci.*, 2008, **254**, 2441.
18 P. Mills and J. L. Sullivan, *Appl. Phys.*, 1983, **16**, 723.
19 (*a*) Y. Mizokawa, *J. Vac. Sci. Technol., A*, 1987, **5**, 2809; (*b*) J. Diaz, G. Paolicelli, S. Ferrer and F. Comin, *Phys. Rev. B: Condens. Matter Mater. Phys.*, 1996, **54**, 8064; (*c*) P. Merel, M. Tabbal, M. Chaker, S. Moisa and J. Margot, *Appl. Surf. Sci.*, 1998, 105; (*d*) V. Chandra, J. Park, Y. Chun, J. W. Lee, I. C. Hwang and K. S. Kim, *ACS Nano*, 2010, **4**, 3979.
20 M. Hu, A. A. Belik, M. Imura, K. Mibu, Y. Tsujimoto and Y. Yamauchi, *Chem. Mater.*, 2012, **24**, 2698.
21 L. Zhang, H. B. Wu and X. W. Lou, *J. Am. Chem. Soc.*, 2013, **135**, 10664.
22 (*a*) Y. Hou, T. Huang, Z. Wen, S. Mao, S. Cui and J. Chen, *Adv. Energy Mater.*, 2014, **4**, 1400337; (*b*) Z. He, J. L. Maurice, A. Gohier, C. S. Lee, D. Pribat and C. S. Cojocaru, *Chem. Mater.*, 2011, **23**, 5379.
23 (*a*) Y. Wu, P. Zhu, M. V. Reddy, B. V. Chowdari and S. Ramakrishna, *ACS Appl. Mater. Interfaces*, 2014, **6**, 1951; (*b*) I. T. Kim, A. Magasinski, K. Jacob, G. Yushin and R. Tannenbaum, *Carbon*, 2013, **52**, 56.
24 (*a*) Y. Li, C. Zhu, T. Lu, Z. Guo, D. Zhang, J. Ma and S. Zhu, *Carbon*, 2013, **52**, 565; (*b*) H. Zhang, L. Zhou, O. Noonan, D. J. Martin, A. K. Whittaker and C. Yu, *Adv. Funct. Mater.*, 2014, **24**, 4337; (*c*) Z. Wang, D. Luan, S. Madhavi, Y. Hu and X. W. Lou, *Energy Environ. Sci.*, 2012, **5**, 5252; (*d*) G. W. Zhou, J. Wang, P. Gao, X. Yang, Y. S. He, X. Z. Liao, J. Yang and Z. F. Ma, *Ind. Eng. Chem. Res.*, 2013, **52**, 1197; (*e*) H. Zhang, L. Zhou and C. Yu, *RSC Adv.*, 2014, **4**, 495.
25 M. M. Thackeray, W. I. F. David and J. B. Goodenough, *Mater. Res. Bull.*, 1982, **17**, 785.
26 H. Lindstrom, S. Sodergren, A. Solbrand, H. Sensmo, J. Hjelm, A. Hagfldt and S. E. Lindquist, *J. Phys. Chem. B*, 1997, **101**, 7717.

